



VICTORIA UNIVERSITY
MELBOURNE AUSTRALIA

A new 3D printed radial flow-cell for chemiluminescence detection: Application in ion chromatographic determination of hydrogen peroxide in urine and coffee extracts

This is the Accepted version of the following publication

Gupta, V, Mahbub, Parvez, Nesterenko, PN and Paull, B (2018) A new 3D printed radial flow-cell for chemiluminescence detection: Application in ion chromatographic determination of hydrogen peroxide in urine and coffee extracts. *Analytica Chimica Acta*, 1005. 81 - 92. ISSN 0003-2670

The publisher's official version can be found at
<https://www.sciencedirect.com/science/article/pii/S0003267017314629>
Note that access to this version may require subscription.

Downloaded from VU Research Repository <https://vuir.vu.edu.au/37252/>

1 **A New 3D Printed Radial Flow-Cell for Chemiluminescence**
2 **Detection: Application in Ion Chromatographic Determination of**
3 **Hydrogen Peroxide in Urine and Coffee Extracts.**

4 Vipul Gupta^{a, b}, Parvez Mahbub^a, Pavel N. Nesterenko^a, Brett Paull^{a, b*}

5 *^aAustralian Centre for Research on Separation Sciences (ACROSS), School of*
6 *Physical Sciences, University of Tasmania, Sandy Bay, Hobart 7001, Tasmania,*
7 *Australia*

8 *^bARC Centre of Excellence for Electromaterials Science, School of Physical Sciences,*
9 *University of Tasmania, Sandy Bay, Hobart 7001, Tasmania, Australia*

10

11

12 **AUTHOR INFORMATION**

13 **Corresponding Author*

14 Brett.Paull@utas.edu.au

15 +61 3 6226 6680

16 Australian Centre for Research on Separation Sciences (ACROSS), School of Physical
17 Sciences, University of Tasmania, Sandy Bay, Hobart 7001, Tasmania, Australia.

18

19 **1 ABSTRACT**

20 A new polymer flow-cell for chemiluminescence detection (CLD) has been designed
21 and developed by diverging multiple linear channels from a common centre port in a
22 radial arrangement. The fabrication of radial flow-cell by 3D PolyJet printing and
23 fused deposition modeling (FDM) has been evaluated, and compared with a similarly
24 prepared spiral flow-cell design commonly used in chemiluminescence detectors. The
25 radial flow-cell required only 10 hours of post-PolyJet print processing time as
26 compared to ca. 360 hours long post-PolyJet print processing time required for the
27 spiral flow-cell. Using flow injection analysis, the PolyJet 3D printed radial flow-cell
28 provided an increase in both the signal magnitude and duration, with an average
29 increase in the peak height of 63% and 58%, peak area of 89% and 90%, and peak
30 base width of 41% and 42%, as compared to a coiled-tubing spiral flow-cell and the
31 PolyJet 3D printed spiral flow-cell, respectively. Computational fluid dynamic (CFD)
32 simulations were applied to understand the origin of the higher CLD signal obtained
33 with the radial flow-cell design, indicating higher spatial coverage near the inlet and
34 lower linear velocities in the radial flow-cell. The developed PolyJet 3D printed radial
35 flow-cell was applied in a new ion chromatography chemiluminescence based assay
36 for the detection of H₂O₂ in urine and coffee extracts.

37

38 **KEYWORDS**

39 Radial flow-cell; 3D printed flow-cell; hydrogen peroxide; Flow injection analysis;
40 chemiluminescence detection; Ion chromatography

41 **ABBREVIATIONS**

42 IC: Ion chromatography

- 43 CLD: Chemiluminescence detection
- 44 PMT: Photomultiplier tube
- 45 CFD: Computational fluid dynamic
- 46 IC-CLD: Ion chromatography coupled chemiluminescence detection
- 47 FDM: Fused deposition modeling
- 48 RANS: Reynolds-averaged Navier–Stokes (RANS)
- 49 SST: Shear stress transport
- 50 FOX: Ferrous oxidation-xylene orange
- 51

52 2 INTRODUCTION

53 Chemiluminescence detection (CLD) is a potential option for the sensitive
54 determination of solutes which do not possess a strong chromophore or fluorophore,
55 which has been used for various applications including clinical, agricultural, to
56 industrial analysis [1-3]. CLD systems have the advantage of requiring relatively
57 simple instrumentation and can offer extremely high sensitivity for certain solutes. A
58 CLD system essentially consists of only two components, (1) a transparent reaction
59 vessel or a flow-cell and (2) a photodetector. The design of CLD flow-cell defines the
60 sensitivity and reproducibility of the detector, as it influences fluid mixing, band
61 dispersion, the amount of emitted light transmitted to the detector, and
62 consequentially the signal magnitude and duration [4]. A flow-cell design which
63 provides these signal enhancements also enables detector miniaturisation by enabling
64 the use of low-cost digital imaging detectors, as compared to expensive high
65 sensitivity photomultiplier tubes.

66

67 Usually, CLD flow-cells are produced by simply coiling polymeric or glass tubing in
68 a plane [4-6] or by milling/etching channels into polymeric materials [7-10]. Coiled-
69 tubing based flow-cells have been widely used for CLD in flow injection analysis
70 (FIA) manifolds [11-14]. However, these simple approaches have some
71 disadvantages, including the rigid nature of most suitable tubing, making the
72 formation of the flat spiral cell rather difficult and irreproducible [15]. Greater design
73 flexibility and complexity can be achieved with the use of milling or etching
74 techniques, with these techniques also providing greater fabrication reproducibility,
75 and access to a wider range of materials. However, they have some notable
76 limitations, including limited resolution of closely spaced channels, and inability to

77 produce complex 3D channel geometries. Such techniques are also not able to
78 produce sealed channels, and thus are rather laborious and time consuming, due to the
79 multiple steps required for the production of the sealed device.
80
81 However, these limitations can potentially be overcome with the use of 3D printing
82 techniques, which can provide rapid and simple production of complex CLD flow-
83 cells in a variety of materials. With the continual development of higher resolution 3D
84 printers allowing multi-material printing, these capabilities are expanding rapidly. In
85 terms of the advantages over other fabrication methods, 3D printing offers (1) the
86 ability to print complex three-dimensional architectures, (2) low cost and time
87 efficient production, (3) minimum wastage of material, (4) a “fail fast and often”[16]
88 approach to prototyping, customisation, and testing, and (5) fabrication of
89 monolithically integrated systems. Accordingly, 3D printing is rapidly becoming a
90 method of choice for both research and industrial fabrication of polymeric and metal
91 based macro- and micro-fluidic devices [17-19]. Use of 3D printing in the production
92 of CLD flow-cells has been recently investigated by Spilstead et al. [20]. However, in
93 this preliminary work, due to the tortuous nature of the spiral flow-cell design
94 investigated, the 3D printing process resulted in only partially cleared (of support
95 material) internal channels [20]. This resulted in significant flow-cell staining, which
96 was presumed to be due to the formation of Mn(IV) on the remaining wax support
97 material in the channels. Accordingly, to obtain the support material free channels,
98 they had to print incomplete channels, and later seal them with transparent films[20].
99 This obviously negated one of the core advantages of 3D printing and illustrated
100 unsuitability of tortuous flow-cell designs in allowing 3D printing fabrication of
101 analytical flow-cells.

102

103 Many varied CLD flow-cell designs have been reported to-date, and the following
104 represents some of the key designs investigated/developed: (1) the most commonly
105 used spirally coiled tubing based flow-cell by Rule et al. [6]; (2) the fountain flow-cell
106 design by Scudder et al. [21], where fluid radially flows between two parallel plates
107 without any channels; (3) the sandwich flow-cell by Pavón et al. [22], which is a
108 membrane based flow-cell; (4) liquid core waveguide based luminescence detectors
109 by Dasgupta et al. [23], which utilise fluoropolymer tubing; (5) the bundle flow-cell
110 by Campíns-Falcó et al. [24], which is based on the random packing of a tube; (6) the
111 vortex flow-cell by Ibáñez-García et al. [25], which consists of a micromixer based
112 on a vortex structure; (7) the serpentine flow-cell by Terry et al. [10], which consists
113 of reversing turns, and finally (8) the droplet flow-cell by Wen et al. [26], which is
114 based on the formation of a small droplet in front of the photodetector.

115

116 Many of the above mentioned flow-cell designs, including the spiral, serpentine, and
117 bundle flow-cells, exhibit complex and tortuous geometries, which would present
118 similar difficulties in terms of 3D printing based fabrication as those discussed above
119 [20]. Whereas, simpler flow-cell designs, such as the fountain flow-cell has resulted
120 in inferior CLD performance with a lower signal intensity and a poor signal
121 reproducibility [10]. These issues suggest the need for a new CLD flow-cell design,
122 which is less tortuous than the conventional flow-cells, enabling 3D printing, while
123 still providing a reproducibly response, ideally of higher signal magnitude and
124 duration to the above alternative designs. Thus herein, a new flow-cell has been
125 designed, developed, and evaluated in comparison with the most commonly used
126 spiral flow-cell design for CLD. The new flow-cell has been designed by diverging

127 multiple linear channels from a common centre port in a radial arrangement and hence
128 named as a 'radial' flow-cell. This radial flow-cell has been produced using both
129 'PolyJet' and fused deposition modeling (FDM) 3D printing techniques. It has been
130 evaluated and compared quantitatively to a similarly proportioned spiral flow-cell
131 design on the basis of (1) simplicity of fabrication with the 3D PolyJet printing and
132 the FDM printing techniques and (2) CLD performance using the cobalt catalysed
133 reaction of H₂O₂ with luminol as the model system. The flow behaviour in the radial
134 flow-cell and spiral flow-cell designs have been simulated through computational
135 fluid dynamic (CFD) calculations to understand the underlying mechanism for the
136 observed differences in the CLD signals obtained. Finally, to investigate the practical
137 application of the developed radial flow-cell, it was evaluated within an ion
138 chromatographic based assay for the analysis of H₂O₂ in urine and coffee extract.

139

140 **3 MATERIALS AND METHODS**

141

142 **3.1 Materials**

143 Luminol (Sigma-Aldrich, MO, USA), CoCl₂ (Univar, IL, USA), Na₃PO₄ 7H₂O
144 (Mallinckrodt, Surrey, UK), NaOH (BDH, PA, USA), H₂O₂ (Chem-Supply Pty Ltd,
145 South Australia, Australia), 5-sulphosalicylic acid (Sigma-Aldrich, MO, USA),
146 ferrous ammonium sulphate (FeSO₄(NH₄)₂SO₄.6H₂O) (England, UK), H₂SO₄ (Merck,
147 VIC, Australia), xylenol orange (Sigma-Aldrich, MO, USA), Sorbitol (BDH, PA,
148 USA), 0.45 μM PTFE captiva syringe filters (Agilent, CA, USA). Deionised water
149 purified through a Milli-Q water purification system (Millipore, MA, USA) with a
150 final resistance of 18.2 MΩ was used for all preparations unless mentioned otherwise.

151

152 **3.2 3D printing**

153 The flow-cells and the black boxes were designed with the Solidworks 3D modelling
154 and CAD software 2014-2015 (Dassault Systèmes SE, France). The PolyJet printed
155 flow-cells were fabricated using an Eden 260VS PolyJet 3D printer (Stratasys, VIC,
156 Australia) with VeroClear-RGD810 resin (Stratasys, VIC, Australia) as the build
157 material and SUP707 (Stratasys, VIC, Australia) as the support material. Post-PolyJet
158 printing, the support material was removed by soaking and intermittent sonication of
159 the flow-cells in a 2% w/v NaOH solution. The FDM printed flow-cells and the black
160 boxes were fabricated using a Felix 3.0 Dual Head FDM 3D printer (IJsselstein,
161 Netherlands) using clear ABS and black PLA filament (Matter Hackers, CA, USA),
162 respectively.

163

164 **3.3 UV-VIS spectroscopy**

165 UV-VIS spectroscopy was performed on the PolyJet printed chips using SP8001 UV-
166 VIS spectrophotometer (Metertech, Taipei, Taiwan). Rectangular chips were designed
167 and printed to fit inside a standard quartz cuvette filled with Millipore water. The UV-
168 VIS spectroscopy was performed from 200 nm to 1000 nm and the transmittance was
169 recorded while using Millipore water as the blank.

170

171 **3.4 Flow injection analysis based chemiluminescence setup**

172 A FIA setup for the CLD of H₂O₂ was established using an in-house built pneumatic
173 assembly for pumping the sample carrier (water) and the reagent (luminol-Co(II))
174 streams, a six port injection valve (VICI Valco, TX, USA) with 2 μL injection loop, a
175 MINIPULS 3 peristaltic pump (Gilson, WI, USA) to fill the injection loop with the
176 sample (H₂O₂), a T-piece to mix the reagent with the sample, 1/16" OD and 0.008" ID

177 PTFE tubing (IDEX Health & Science (Kinesis), Qld, Australia), and short tefzel nut
178 1/16 black (IDEX Health & Science (Kinesis), Qld, Australia). Each flow-cell and a
179 R960 Photomultiplier tube (PMT) (Hamamatsu (Stantron), NSW, Australia) were
180 enclosed in a light tight dark box. The PMT signal was recorded with respect to time
181 through a Powerchrome 280 system (eDAQ, NSW, Australia) by converting the
182 produced current into voltage through an online resistor. The luminol-Co(II) reagent
183 was prepared as described previously [27].

184

185 **3.5 *Computational fluid dynamic simulations***

186 Computational fluid dynamic simulations were performed using ANSYS 17.0
187 software with CFX solver. The radial and spiral flow-cell designs were meshed
188 similarly, resulting in the number of nodes as 4 million and 6 million, respectively.
189 Reynolds-averaged Navier–Stokes (RANS) simulations were performed using the
190 shear stress transport (SST) turbulence model with water as the fluid material. A no-
191 slip wall condition with a roughness of 20 μm was prescribed for the walls. The
192 iterations were manually observed for the convergence of the turbulence kinetic
193 energy, velocity, pressure, and shear stress user points. On successful completion of
194 each run, the results were analysed as required with the CFX-Post.

195

196 **3.6 *FOX assay***

197 A ferrous oxidation-xylenol orange (FOX) assay reagent was prepared following the
198 recipe reported by Yuen et al.[28]. Briefly, 1 mL of ferrous ammonium sulphate
199 solution was mixed with 100 mL of xylenol orange-sorbitol solution. The ferrous
200 ammonium sulphate solution was prepared by dissolving 25 mM ferrous ammonium
201 sulphate in 2.5 M H_2SO_4 . The xylenol orange-sorbitol solution was prepared by

202 dissolving 125 μM of xylenol orange and 100 mM of sorbitol in water. The FOX
203 reagent was freshly prepared just before each analysis. The FOX assay itself involved
204 adding 100 μL of a sample to 1 mL of the FOX reagent into 2 mL amber coloured
205 centrifuge vials (Eppendorf, Hamburg, Germany), which were incubated at room
206 temperature for 20 min (Pierce Chemical Company, Rockford, USA). The absorbance
207 of each sample at 560 nm was measured against a reference blank using the above-
208 mentioned UV-VIS spectrophotometer.

209

210 **3.7 Ion chromatography**

211 The chromatographic analysis was performed using Waters Alliance 2695 HPLC
212 system (Waters, MA, USA), controlled with Empower Pro software using IonPac®,
213 using the following columns: IonPac CG10 (column size: 50 x 4 mm ID, particle size:
214 8.5 μm), IonPac CG11 (column size: 50 x 2 mm ID, particle size: 7.5 μm), and
215 IonPac CS11 (column size: 250 x 2 mm ID, particle size: 7.5 μm) (Thermo Fisher
216 Scientific, MA, USA). The column temperature was maintained at 24 °C and the
217 sample temperature was maintained at 4 °C. An injection volume of 10 μL was used.
218 Isocratic separation of H_2O_2 was performed using 100% water as the mobile phase at
219 a flow rate of 800 $\mu\text{L min}^{-1}$ and a 5 min post-run clean-up was performed with 100
220 mM NaCl at a flow rate of 1 mL min^{-1} . UV detection was performed with Waters 996
221 PDA detector (Waters, MA, USA) at 210 nm. CLD was performed as described
222 above. Both UV and CLD were performed during separate runs to prevent any
223 degradation of H_2O_2 due to UV exposure. A pneumatic pressure of 200 kPa ($\sim 800 \mu\text{L}$
224 min^{-1}) was used for the luminol-Co(II) reagent stream.

225

226 **3.8 *Urine analysis***

227 On spot midstream urine samples were collected from a non-fasting healthy
228 individual male and were analysed within 30 mins (including pre-sample treatment).
229 Urine samples were collected in an aluminium foil lined 20 mL glass vial, and were
230 centrifuged and protein precipitated in 2 mL amber centrifuge vials. Centrifugation
231 was performed in an Eppendorf 5424 centrifuge (Eppendorf, Hamburg, Germany).

232

233 **3.9 *Coffee analysis***

234 Freshly grounded coffee beans were extracted on a Café Espresso II coffee machine
235 (Sunbeam, NSW, Australia), using 19 g of coffee powder and made to a final volume
236 of 220 mL. Coffee was brewed in drinking water following the same procedure as
237 typically used to make coffee. Coffee samples were analysed immediately, without
238 any further treatment.

239

240 **4 RESULTS AND DISCUSSION**

241

242 **4.1 *Flow-cell designs***

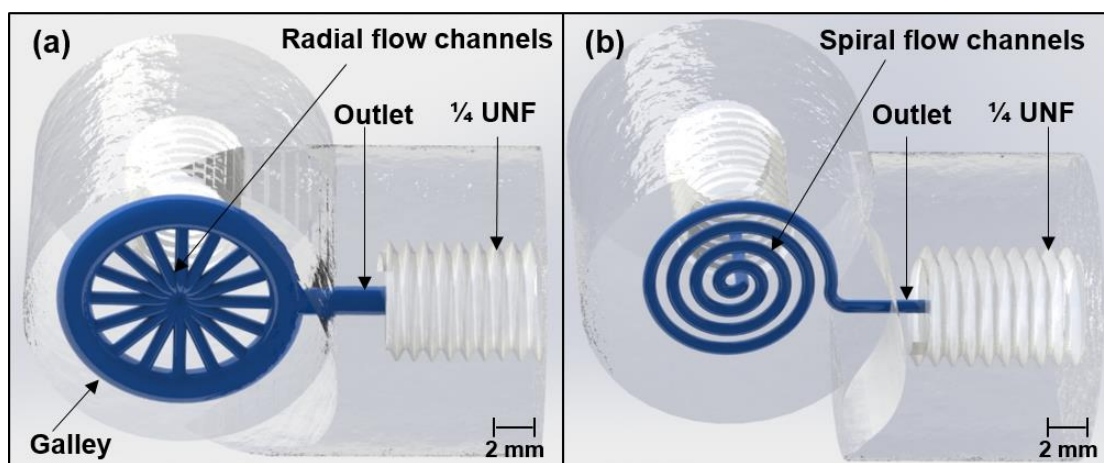
243 The radial flow-cell was developed by arranging 16 channels in a parallel radial
244 arrangement as shown in Figure 1 (a). All channels were designed with a 700 μm ID
245 and were connected to a common inlet at the centre and a common outlet galley of
246 1800 μm ID at the circumference. The galley exited with a single outlet of 1500 μm
247 ID. The galley and outlet dimensions were optimised empirically with the help of
248 computational fluid dynamic (CFD) simulations and visual inspection, by pumping a
249 food dye, to prevent any re-circulation from the galley into the channels. Each
250 individual channel consisted of (1) a 3.63 mm long linear section and (2) a 1.62 mm

251 long curved section with a fillet radius of 1.5 mm near the inlet and a total flow-cell
252 volume of 32 μL as shown in Figure 1 (a). The channel lengths were designed to
253 completely occupy the PMT window, and the galley was kept out of the PMT
254 window. A bottom layer of 1 mm thickness was included to provide robustness,
255 allowing the use of flow-cells up to at least a pressure of 2 MPa. Both the inlet and the
256 outlet were connected to a $\frac{1}{4}$ unified fine pitch thread (UNF) port to enable a unibody
257 design and allow their easy assembly and disassembly within any conventional FIA
258 manifold.

259

260 A conventional coiled-tubing flow-cell was fabricated by spirally coiling a $\frac{1}{16}$ " OD
261 and 0.02" ID PTFE tubing within a circular diameter of 10 mm and a total flow-cell
262 volume of 13 μL . The coiled-tubing based flow-cell was glued to a black platform,
263 which was trimmed to fit in a similar black box as used with the 3D printed flow-cells
264 as described below. Additionally, a spiral flow-cell design with the similar outer
265 diameter and the number of turns as of the coiled-tubing flow-cell was developed for
266 3D printing, as shown in Figure 1 (b), to allow closer comparison with the radial
267 flow-cell. The 3D printed spiral flow-cell was developed using an Archimedes spiral
268 with an inner diameter of 1 mm, an outer diameter of 10 mm, a pitch of 1.20 mm, and
269 a total flow-cell volume of 25 μL . The channel inner diameter, outer diameter, and the
270 bottom layer thickness of the spiral flow-cell were kept as similar as possible to the
271 radial flow-cell. The spiral was connected to an inlet at the centre and an outlet at the
272 end. Both the inlet and the outlet were again connected to a $\frac{1}{4}$ UNF threaded port.

273



274

275 Figure 1. Chemiluminescence flow-cells: (a) render of the 3D printed radial flow-cell
 276 and (b) render of the 3D printed spiral flow-cell.

277

278 4.2 3D printing

279 Two complimentary 3D printing techniques, namely PolyJet printing and FDM were
 280 applied to the fabrication of radial and spiral flow-cells. The PolyJet printing
 281 technique utilises foreign support material and hence allows fabrication of complex
 282 structures, whereas, the FDM printing technique can be used without any support
 283 material, allowing easy fabrication of simple structures. The use of PolyJet printing
 284 for the production of a spiral flow-cell has been previously discussed by Spilstead et
 285 al. [20]. They highlighted the issue of incomplete removal of the wax support material
 286 from the flow channels as mentioned above. In the current work, this limitation was
 287 overcome with the use of a water-soluble support material, namely SUP707. Use of
 288 the SUP707 support material as opposed to the wax support material facilitated its
 289 complete removal from the tortuous flow channels. However, complete removal of
 290 the support material from the 3D printed spiral flow-cell required soaking and
 291 intermittent sonication in a 2% (w/v) NaOH solution for ca. 360 hours. This lengthy
 292 cleaning protocol enabled the direct formation of closed and completely clear flow-

293 cell channels. Complete removal of the support material was confirmed by visual
294 inspection, lack of channel staining, and a reproducible signal from successive
295 injections of H₂O₂.

296

297 As compared to the spiral design, the radial flow-cell was found to be free of any
298 support material within 10 hours, applying the same post-processing protocol. The
299 significant reduction in time required for removal of the support material from the
300 radial flow-cell was facilitated by the linear configuration of the channels, the
301 presence of wide galley providing additional solvent reserve in the flow-cell, the
302 availability of two entry points for the solvent into each channel that are inlet and
303 galley, and the parallel arrangement of the channels allowing simultaneous cleanup of
304 multiple channels. These features allowed successful 3D fabrication of the radial
305 flow-cell with flow channels of less than 500 μm ID, whereas a spiral flow channel of
306 less than 700 μm ID required more than a month to fully remove the water soluble
307 support material. This greatly reduced post-processing time enabled the entire process
308 of fabrication and post-processing to be accomplished in under a day. Attempting the
309 fabrication of the 700 μm ID spiral flow-cell with an FDM printer resulted in
310 complete channel collapse and blockage, whereas FDM fabrication of the 700 μm ID
311 radial flow-cell resulted in a successful print with open channels.

312

313 ***4.3 PolyJet printed chemiluminescence detection flow-cells***

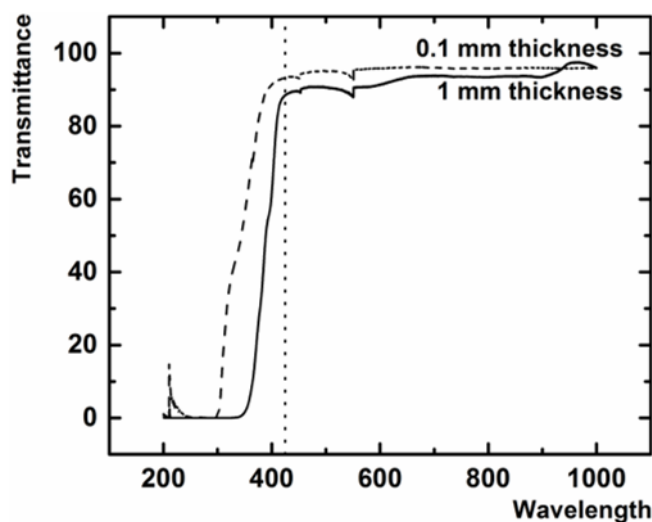
314 PolyJet printing was the only technique that allowed successful fabrication of both the
315 radial and spiral flow-cells. Accordingly, the PolyJet printed flow-cells were used for
316 the remainder of the study. The optical transmittance of PolyJet printed chips was
317 studied to evaluate the suitability of PolyJet printed flow-cells for the CLD of H₂O₂

318 using luminol-Co(II) reagent. The chemiluminescence emission wavelengths from the
319 H₂O₂ and luminol-Co(II) reaction range from 380 nm to 600 nm [29]. Accordingly,
320 the transmittance of PolyJet printed chips was recorded for wavelengths ranging from
321 200 nm to 1000 nm. As shown in Figure 2, 1 mm and 100 μm thick PolyJet printed
322 chips resulted in 89% and 94% transmittance, respectively at 430 nm (highest
323 emission wavelength of H₂O₂-luminol-Co(II) chemiluminescence reaction [29]). The
324 transparency of these flow-cells can be further improved in future through various
325 surface treatments such as polishing, polydimethylsiloxane coating, polystyrene
326 coating, etc. [30]. PolyJet printed flow-cells were transparent in nature and lacked any
327 reflective or opaque backing. Accordingly, black boxes were designed for each flow-
328 cell to (1) provide an opaque backing, (2) ensure a light tight environment around the
329 flow-cell and the PMT, and (3) closely align the flow-cell and the PMT. The black
330 box was designed and 3D printed in two parts (a top and a bottom half) with negative
331 contours to that of the respective flow-cell, as shown in the Supporting information
332 Figure S-1. Holders were included for the PMT and the screws. Both parts were
333 sealed together through a 3D printed lego-type interlock between them. A tight seal
334 was observed between the two halves of the black box and the black box, the flow
335 cell, and the PMT.

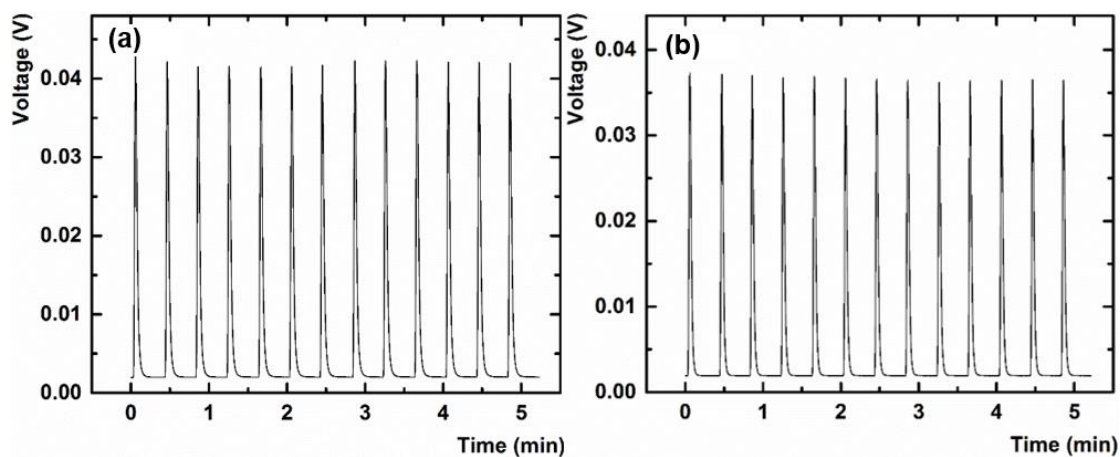
336

337 The PolyJet resin used in this work was an acrylate based polymer composed of
338 complex mixture of monomers including exo-1,7,7-trimethylbicyclo[2.2.1]hept-2-yl
339 acrylate or acrylic acid isobornyl ester (CAS 5888-33-5, 20-30%); tricyclodecane
340 dimethanol diacrylate (CAS 42594-17-2, 15-30%); 2-hydroxy-3-phenoxypropyl
341 acrylate (CAS 16969-10-1), 4-(1-oxo-2propenyl)morpholine (CAS 5117-12-4);
342 Bisphenol A containing acrylate oligomer treated with epichlorohydrin (5-15%), and

343 2,4,6-trimethylbenzoyldiphenylphosphine oxide as photoinitiator (0.1-2%) [31]. The
344 polyacrylates should provide reasonable chemical resistance to most dilute acids,
345 bases and oils. However, their use with organic solvents is not recommended as per
346 the known incompatibilities of acrylates with organic solvents. Repetitive injections
347 of 10 μM H_2O_2 at a rate of 150 injections per hour resulted in reproducible
348 chemiluminescence signal with an RSD (n=13) of 1.01% and 0.91% with the use of
349 the 3D printed radial flow-cell and the 3D printed spiral flow-cell, respectively as
350 shown in Figure 3. This indicates the absence of any flow-cell staining or carryover
351 effects, and an ability to perform high throughput CLD studies with the use of these
352 3D printed flow-cells. In terms of stability, no visible signs of damage were observed
353 to either the 3D printed spiral or 3D printed radial flow-cells throughout this entire
354 study, which was performed over a period of more than one year, with more than
355 1000 injections on each flow-cell.
356



357
358 Figure 2. UV-VIS transmittance of the PolyJet 3D printed 1 mm and 0.1 mm thick
359 chips.
360



361

362 Figure 3. Successive FIA injections of 10 μM H_2O_2 using the PolyJet 3D printed (a)

363 radial flow-cell and (b) spiral flow-cell.

364

365 4.4 Chemiluminescence system optimisation

366 An FIA-chemiluminescence system was setup as shown in Figure 4 (a). Its various

367 parameters were optimised to obtain the maximum reproducible signal intensity.

368 Following our previous work [32], 50 mM Na_3PO_4 at pH 12 was used to prepare the

369 luminol-Co(II) chemiluminescence reagent. Following the previous work of

370 Greenway et al. [33] and Marle et al. [34], 10 μM CoCl_2 solution was used to obtain

371 the maximum reproducible signal intensity while avoiding any precipitation. The

372 luminol concentration and the carrier/reagent flow rate ratio were optimised

373 experimentally through iterative univariate analysis since their optimum values were

374 mutually dependent. This provided an optimum luminol concentration of 0.29 mM as

375 shown in Figure 4 (b) and an optimum pneumatic pressure ratio of 1.4 as shown in

376 Figure 4 (c). Accordingly, a luminol-Co(II) solution with 0.29 mM luminol and 10

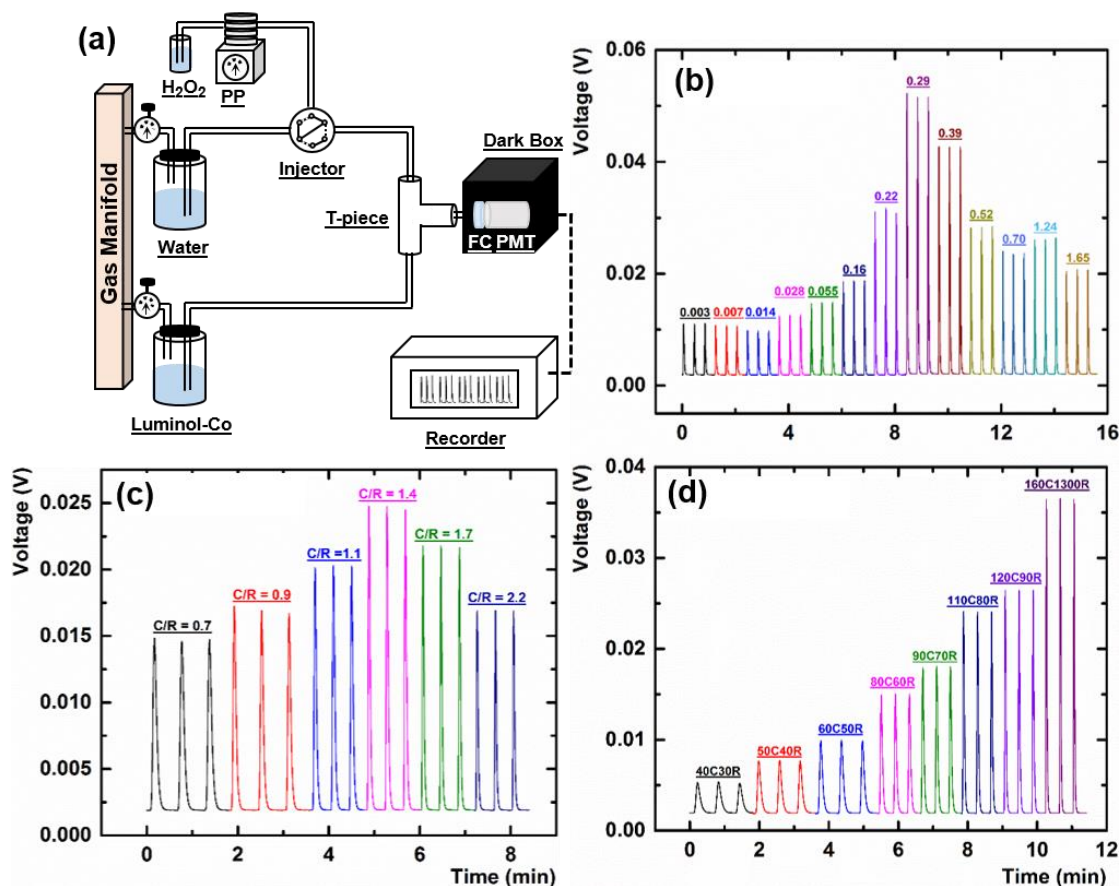
377 μM CoCl_2 solution in 50 mM Na_3PO_4 buffer with pH 12 was used as the

378 chemiluminescence reagent. As shown in Figure 4 (d), the maximum reproducible

379 signal intensity was observed at the highest total (carrier stream + reagent stream)

380 flow rate. This is presumably due to (1) the higher resultant turbulence at the T-piece,

381 which facilitates better mixing of the sample and the reagent and (2) rapid transfer of
 382 the chemiluminescence products from the T-piece to the flow-cell. Accordingly, a
 383 pneumatic pressure of 160 kPa was used for the carrier stream. As per the optimised
 384 carrier/reagent pneumatic pressure ratio of 1.4, the reagent stream pneumatic pressure
 385 should be 114 kPa. However, the here used pneumatic assembly only allowed to
 386 reproducibly obtain pressures in the integer multiples of 10. Hence, pneumatic
 387 pressures of 110 kPa, 120 kPa, and 130 kPa were investigated for the reagent stream.
 388 No significant difference in the signal intensity was observed between these three
 389 reagent stream pneumatic pressures, however, a slightly better reproducibility was
 390 observed at 130 kPa. The total volumetric flow rate (carrier + reagent) was observed
 391 to be ca. $800 \mu\text{L min}^{-1}$. The initial optimisation studies were performed with the 3D
 392 printed spiral flow-cell and the final results were verified for all three types of flow-
 393 cells.



394

395 Figure 4. Chemiluminescence FIA system: (a) schematic of the experimental FIA
396 CLD setup (PP – peristaltic pump, FC – flow-cell), (b) observed chemiluminescence
397 peaks at different luminol concentrations as indicated in mM for three successive
398 injections, (c) observed chemiluminescence peaks at different carrier/reagent
399 pneumatic pressure ratios as indicated for three successive injections, (d) observed
400 chemiluminescence peaks at different carrier and reagent pneumatic pressures in kPa
401 as indicated by the numeral preceding C and R for the carrier and the reagent streams,
402 respectively for three successive injections.

403

404 **4.5 Chemiluminescence performance**

405 The 3D printed radial flow-cell was compared with both the conventional coiled-
406 tubing spiral flow-cell and the 3D printed spiral flow-cell with regard to analytical
407 performance. All three flow-cells were compared using six different H₂O₂ standard
408 concentrations, namely 100 nM, 200 nM, 400 nM, 800 nM, 1.6 μM, and 3.2 μM, the
409 results from which are included in Figure 5 and Tables 1 and 2, and discussed below.

410

411 CLD using the 3D printed radial flow-cell provided an increase in the peak height (as
412 shown in Figure 5 (a)) and peak area (as shown in the Supporting information (Figure
413 S-2)) for all six H₂O₂ concentrations, as compared to both the coiled-tubing spiral
414 flow-cell and the 3D printed spiral flow-cell. Compared to the coiled-tubing spiral
415 flow-cell, the 3D printed radial flow-cell resulted in an average increase in the peak
416 height of 63.5% and an average increase in the peak area of 89.4% as shown in Table
417 1. Compared to the 3D printed spiral flow-cell, the 3D printed radial flow-cell
418 resulted in an average increase in the peak height of 58.5% and an average increase in
419 the peak area of 89.5% as shown in Table 1. No significant differences in the peak

420 height or the peak area were observed between the coiled-tubing spiral flow-cell and
421 the 3D printed spiral flow-cell. Excellent reproducibility was observed for all three
422 flow-cells based upon three successive injections as shown in Table 1. A maximum
423 RSD of 3.4%, 5.6%, and 3.0% was observed for the 3D printed radial flow-cell, the
424 coiled-tubing spiral flow-cell, and the 3D printed spiral flow-cell, respectively, for the
425 peak representing 100 nM H_2O_2 , again as shown in Table 1.

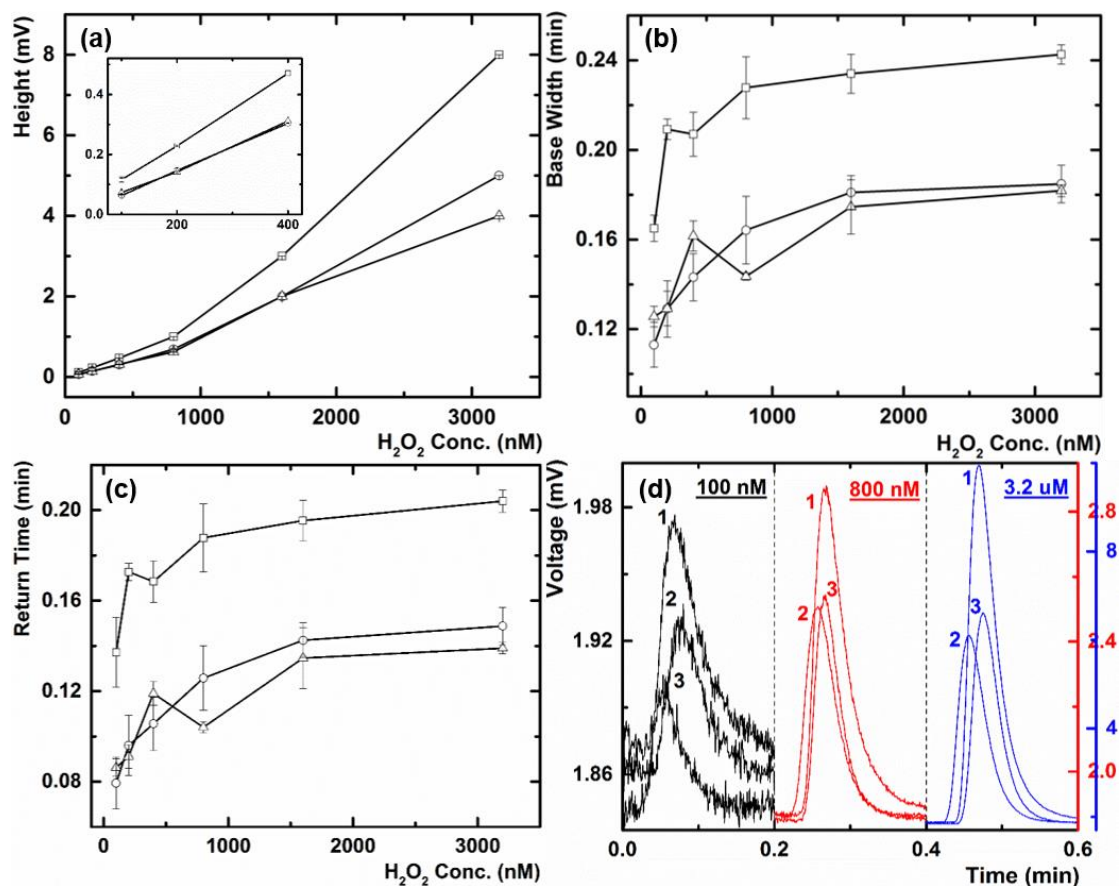
426

427 Along with the peak height and peak area, the 3D printed radial flow-cell also resulted
428 in an increase in the peak width for all six H_2O_2 concentrations as compared to both
429 the other flow-cells, as shown in Figure 5 (b). The 3D printed radial flow-cell resulted
430 in an average increase in the peak width of 41.3% and 42.0% as compared to the
431 coiled-tubing spiral flow-cell, and the 3D printed spiral flow-cell, respectively as
432 shown in Table 1. Again, no significant differences in the peak width were observed
433 between the coiled-tubing spiral flow-cell and the 3D printed spiral flow-cell. An
434 increase in the peak width was the result of an increase in the peak return and not the
435 onset time, hence indicating an increase in the signal duration with the use of the 3D
436 printed radial flow-cell as shown in Figure 5 (c). An onset time of 0.07 min (0.03 min
437 from the injection to the start of the peak and 0.04 min from the start of the peak to
438 the peak maxima) was observed for all three flow-cells at all six H_2O_2 concentrations.
439 Representative chemiluminescence peaks for all three flow-cells at three different
440 H_2O_2 concentrations, namely 100 nM, 800 nM, and 3.2 μM are shown in Figure 5 (d)
441 for visual comparison.

442

443 All three flow-cells resulted in linear calibration plots for the peak height v/s
444 concentration in two distinct regions, namely 100 nM to 400 nM and 800 nM to 3.2

445 μM , each with an $R^2 > 0.99$. As shown in Table 2, the 3D printed radial flow-cell
 446 resulted in a higher sensitivity as compared to both the other flow-cells in both the
 447 above-mentioned regions.
 448



449
 450 Figure 5. Chemiluminescence peak characteristics for the 3D printed radial flow-cell
 451 (\square), the coiled-tubing spiral flow-cell (Δ), and the 3D printed spiral flow-cell (\circ): (a)
 452 peak heights at different H_2O_2 concentrations, the inset shows the magnified view of
 453 the peak height v/s concentration plot for the 100, 200, and 400 nM H_2O_2
 454 concentrations. (b) peak base widths at different H_2O_2 concentrations, (c) peak return
 455 times at different H_2O_2 concentrations, and (d) representative chemiluminescence
 456 peaks at 100 nM, 800 nM, and 3.2 μM as indicated for the 3D printed radial flow-cell
 457 (1), the coiled-tubing spiral flow-cell (2), and the 3D printed spiral flow-cell (3).

458 Note: the chemiluminescence peaks in the sub figure (d) are not perfectly aligned on
 459 the time axis due to their slightly different injection times.

460

461 Table 1. Comparison of the peak characteristics obtained with the 3D printed radial
 462 flow-cell (3DP RFC), the coiled-tubing spiral flow-cell (SFC), and the 3D printed
 463 spiral flow-cell (3DP SFC) at six different H₂O₂ concentrations.

464

H ₂ O ₂ (nM)	Rel. % increase (peak height) using Radial Cell		Rel. % increase (peak area) using Radial Cell		Rel. % increase (peak width) using Radial Cell		% RSD (peak height)		
	Spiral (tube)	Spiral (3D)	Spiral (tube)	Spiral (3D)	Spiral (tube)	Spiral (3D)	3DP Radial	Spiral (tube)	Spiral (3D)
	100	58.1	84.7	20.7	56.6	31.4	46.0	3.4	5.6
200	61.2	55.9	89.1	66.1	62.0	62.2	1.1	1.9	2.4
400	51.0	54.8	77.2	106.1	28.1	44.6	0.79	2.5	0.7
800	60.5	45.3	62.3	140.3	58.7	38.7	<0.01	2.1	2.0
1600	50.0	50.0	80.7	27.1	34.0	29.3	<0.01	<0.01	<0.01
3200	100.0	60.0	206.3	140.7	33.4	31.3	<0.01	<0.01	<0.01

465

466

467 Table 2. Calibration results for the 3D printed radial flow-cell (3DP RFC), coiled-
 468 tubing spiral flow-cell (SFC), and the 3D printed spiral flow-cell (3DP SFC).

Parameter	100-400 nM H ₂ O ₂			800-3200 nM H ₂ O ₂		
	3DP RFC	SFC	3DP SFC	3DP RFC	SFC	3DP SFC
Linear Slope	1.2 × 10 ⁻⁶	7.8 × 10 ⁻⁷	8.0 × 10 ⁻⁷	3.0 × 10 ⁻⁶	1.3 × 10 ⁻⁶	1.9 × 10 ⁻⁶
Y-Intercept	-6.9 × 10 ⁻⁶	-1.0 × 10 ⁻⁵	-1.7 × 10 ⁻⁵	-1.5 × 10 ⁻³	-7.9 × 10 ⁻¹⁴	-1.0 × 10 ⁻³
R²	0.9996	0.9925	0.9999	0.9972	0.9999	0.9999

469

470 **4.6 Computational fluid dynamic simulated flow behaviour**

471 Flow behaviour within the radial and spiral flow-cell designs were simulated and
472 studied using computational fluid dynamic (CFD) calculations. Figures 6 (a) and 6 (b)
473 demonstrates 100 simulated velocity streamlines in the radial flow-cell design and the
474 spiral flow-cell design, respectively. As shown in Figure 6 (a), unidirectional velocity
475 streamlines were observed in the radial flow-cell, originating from the inlet and
476 terminating in the outlet. This indicates that the designed galley diameter of 1800 μm
477 was found sufficient to prevent any recirculation from the galley into the channels.
478 This was further validated through visual inspection by pumping food dye and by the
479 absence of any split or odd chemiluminescence peaks resulting from the use of the 3D
480 printed radial flow-cell.

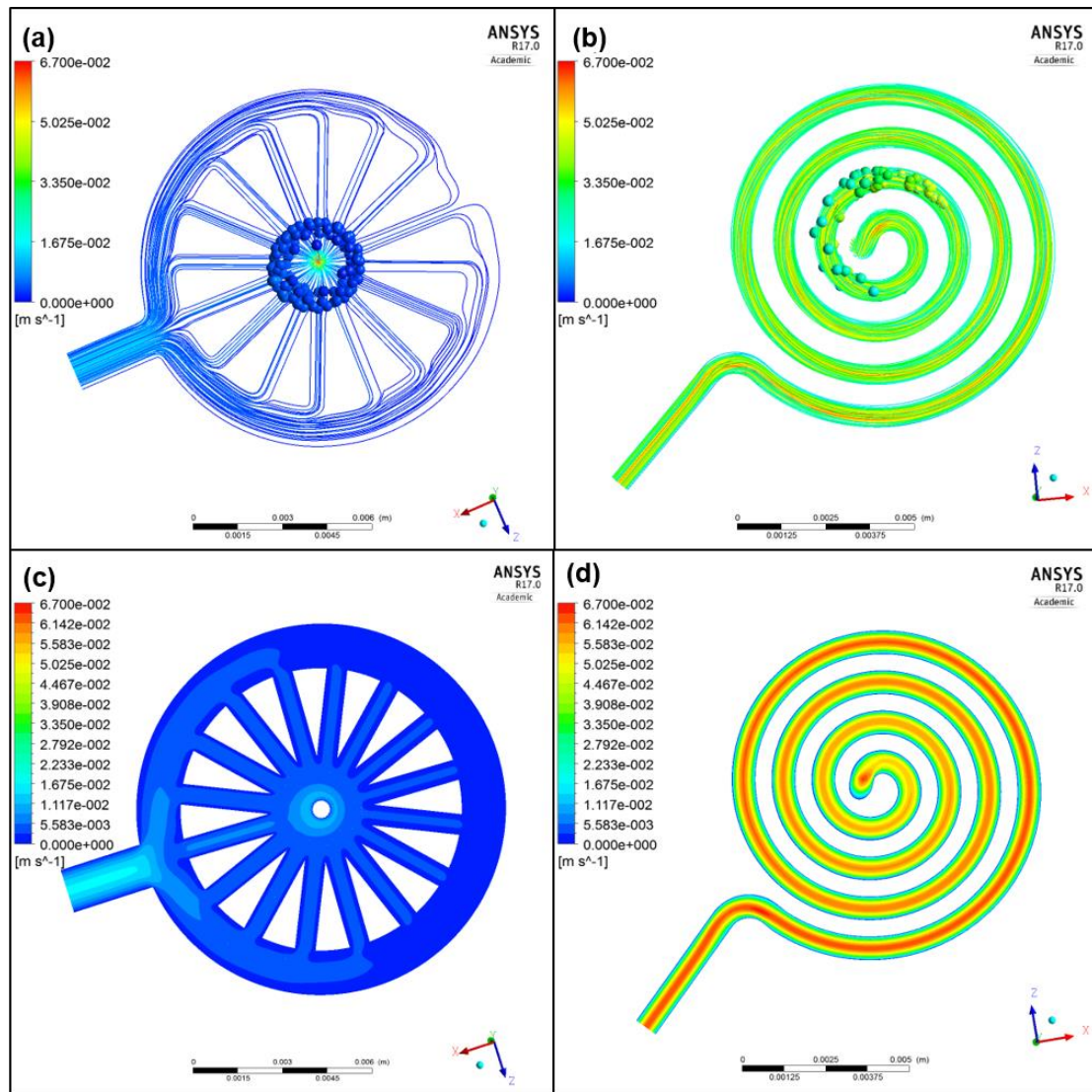
481

482 The simulated fluid flow at the experimental flow rate of 800 μLmin^{-1} in both the
483 radial flow-cell and spiral flow-cell designs was studied to understand the underlying
484 mechanism for the increased response and improved sensitivity of the 3D printed
485 radial flow-cell as compared to the coiled-tubing spiral flow-cell and the 3D printed
486 spiral flow-cell. The respective positions of 100 representative flow streams at 0.25
487 simulated seconds in the radial flow-cell and spiral flow-cell designs are marked by
488 the velocity colour coded balls in Figure 6 (a) and 6 (b), respectively. This indicates
489 dispersion of flow streams over a higher area in the radial flow-cell design as
490 compared to the spiral flow-cell design. Higher dispersion of the flow streams in the
491 radial flow-cell design will enable higher spatial coverage by the generated
492 chemiluminescence products in front of the PMT window. Higher spatial coverage in
493 the radial flow-cell design especially near the inlet should contribute towards a more
494 efficient transfer of the photons from the chemiluminescence reaction to the

495 photodetector, as the chemiluminescence intensity decays with time as per a first
496 order rate equation [35]. Accordingly, this should contribute towards the observed
497 relative increase in the peak area, peak height, and chemiluminescence sensitivity
498 with the 3D printed radial flow-cell. Figures 6 (c) and 6 (d) demonstrate the velocity
499 distributions in the radial flow-cell design and the spiral flow-cell design,
500 respectively. This indicates that the radial flow-cell design results in ca. 10 times
501 smaller linear velocities in the radial flow channels as compared to the spiral flow
502 channel. Smaller linear velocities in the radial flow channels contribute towards the
503 observed increase in the signal duration and a corresponding increase in the peak
504 width [36].

505

506 A non-uniform flow velocity distribution was observed within the radial flow
507 channels. Higher linear velocities were observed in the channels exiting near the
508 outlet as compared to the channels exiting away from the outlet as shown in Figure 6
509 (c). This is due to a differential pressure drop experienced across the galley as shown
510 in the Supporting Information (Figure S-3). This non-uniform flow velocity
511 distribution among the radial flow channels did not result in any observed problems
512 such as irreproducibility or peak distortion. However, the differential pressure drop
513 across the galley and consequentially the non-uniform flow velocity distributions
514 among the radial flow channels can be minimised in future by further optimisation of
515 the galley dimensions and the outlet position. The individual velocity profiles in each
516 radial flow channel and in each spiral turn are shown in the Supporting Information
517 (Figures S-4 and S-5, respectively).



518

519 Figure 6. Computational fluid dynamic (CFD) simulated velocity streams and velocity
 520 contour plots at an inlet flow rate of 800 $\mu\text{L min}^{-1}$: (a) velocity streamlines in the
 521 radial flow-cell design and the representative flow at simulated 0.25 s is marked by
 522 velocity colour coded balls, (b) velocity streamlines in the spiral flow-cell design and
 523 the representative flow at simulated 0.25 s is marked by velocity colour coded balls,
 524 (c) velocity contour plot at mid plane of the radial flow-cell design, and (d) velocity
 525 contour plot at mid plane of the spiral flow-cell design.

526

527 **4.7 Hydrogen peroxide in urine and coffee extracts**

528 An IC-CLD system was developed to provide a fast and automated determination of
529 urinary and coffee extract H₂O₂. It was assembled by substituting the sample carrier
530 line from the T-piece (as shown in Figure 4 (a)) with the outlet from the cation
531 exchange column. The IC method was developed using a cation exchange column
532 packed with a sulphonated cation-exchanger and a water only mobile phase for the
533 separation of H₂O₂ from otherwise interfering sample matrix ions [37]. Three
534 IonPac® cation exchange columns were studied, namely CG10, CG11, and CS11,
535 each with different particle and column sizes as mentioned above, assessing their
536 chromatographic selectivity towards H₂O₂. In terms of overall chromatographic
537 retention and efficiency, the CG10 proved most acceptable and was accordingly used
538 for H₂O₂ separation. The CLD was performed with the above-mentioned luminol-
539 Co(II) reagent using the new 3D printed radial flow-cell.

540

541 Urinary H₂O₂ was first observed by Varma and Devamanoharan [38] in 1990, since
542 then it has been studied by several researchers [39-41]. H₂O₂ has been believed to
543 produce damaging reactive oxygen species in the human body, although it also acts as
544 a signalling molecule to regulate cellular processes [39]. The amount of H₂O₂
545 excreted in urine is linked to several activities [39], such as coffee drinking [42, 43],
546 alcohol consumption [44], and exercise [45], and also several diseases [39], such as
547 cancer [46], diabetes mellitus [47], respiratory distress syndrome [48], intestinal
548 parasitic infection [49], Down's syndrome [50], and total body oxidative stress [28].
549 An increase in urinary H₂O₂ post-coffee drinking is partially linked to direct diffusion
550 of H₂O₂ from coffee into the oral cavity and the upper gastrointestinal tract [51].

551

552 Traditionally, urinary H₂O₂ is measured using either an oxygen selective electrode
553 [52, 53] or the ferrous oxidation-xylenol orange (FOX) assay (and derivatives thereof)
554 [28, 47, 50]. However, oxygen selective electrodes have been found less sensitive for
555 urinary H₂O₂ [54] and suffer from frequent fouling. Additionally, the FOX assay
556 requires a long reaction time of ca. 60 min [28] and manual operation. Accordingly,
557 herein to demonstrate the practical application of the new flow cell and
558 simultaneously provide a potentially beneficial new IC-CLD method for urinary H₂O₂
559 determinations, an IC-CLD system was developed including the new 3D printed
560 radial flow-cell, and applied to H₂O₂ in urine and coffee extracts.

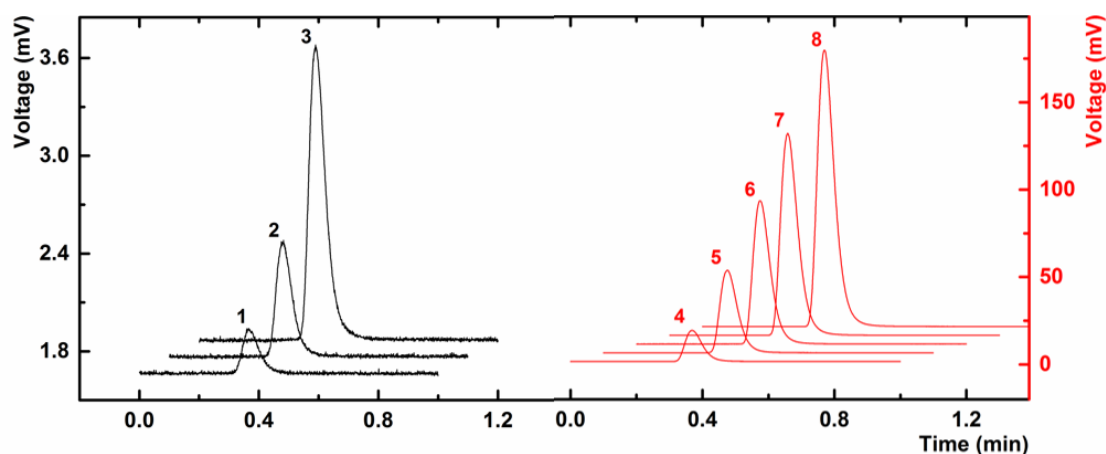
561

562 The developed IC-CLD system resulted in linear calibration plots from 1.25 μM to 5
563 μM H₂O₂ (slope = 3.86×10^{-4} , $R^2 = 0.9953$) and from 20 μM to 100 μM H₂O₂ (slope
564 = 1.78×10^{-3} , $R^2 = 0.9938$). Representative chemiluminescence chromatograms
565 obtained with eight H₂O₂ standards, namely 1.25 μM, 2.5 μM, 5 μM, 20 μM, 40 μM,
566 60 μM, 80 μM, and 100 μM are shown in Figure 7. Peak height %RSDs for the above
567 standards, based upon triplicate injections of each, were 9.19, 3.91, 5.80, 4.68, 2.63,
568 4.38, 1.90, and 1.14, respectively.

569

570 H₂O₂ peaks in the real samples were identified using the retention time of the H₂O₂
571 standards, and by spiking the real samples with known concentrations of H₂O₂. To
572 determine accuracy of the developed IC-CLD system, an unknown sample solution of
573 H₂O₂ was analysed first using a conventional FOX assay, and secondly with the
574 developed IC-CLD system. The FOX assay indicated the concentration of the
575 unknown H₂O₂ sample as 57.8 ± 1.2 μM, using a linear calibration ($R^2 = 0.9846$) plot
576 from 20 μM to 80 μM H₂O₂ ($n = 3$). Using the IC-CLD system, the concentration of

577 the unknown H₂O₂ sample was found as $57.6 \pm 2.1 \mu\text{M}$, here using a linear calibration
578 ($R^2 = 0.9974$) plot from $20 \mu\text{M}$ to $80 \mu\text{M}$ H₂O₂ ($n=3$). Calibration curves for the
579 comparison assays can be found in the supporting information (Figure S-6).
580



581
582 Figure 7. Representative chemiluminescence chromatograms for H₂O₂ standards with
583 the developed IC-CLD system: $1.25 \mu\text{M}$ (1), $2.5 \mu\text{M}$ (2), $5 \mu\text{M}$ (3), $20 \mu\text{M}$ (4), $40 \mu\text{M}$
584 (5), $60 \mu\text{M}$ (6), $80 \mu\text{M}$ (7), and $100 \mu\text{M}$ (8).

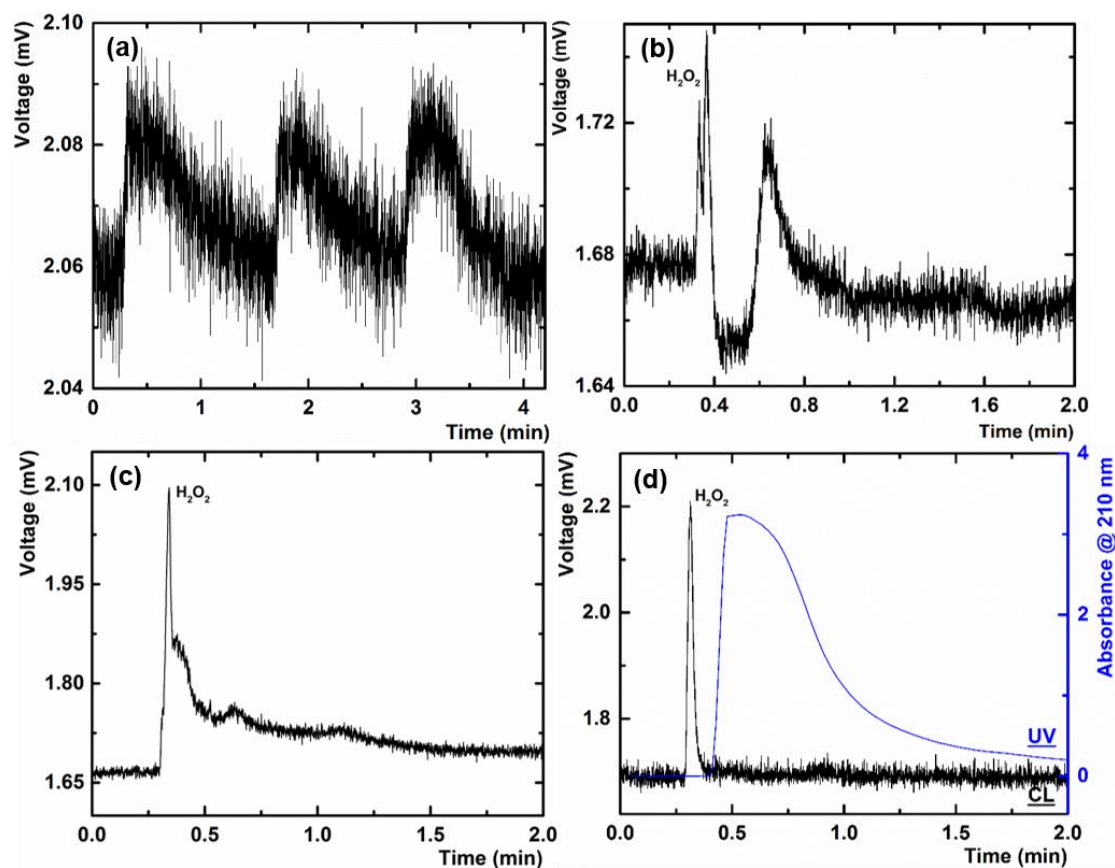
585
586 Analysis of untreated urine samples using FIA resulted in a signal to noise ratio of
587 less than 3, as shown in Figure 8 (a). This low signal to noise ratio was observed
588 presumably due to significant matrix effects. Uric acid was identified as a significant
589 interferent through interference studies. When urine samples were then directly
590 passed through the CG10 column, to separate the H₂O₂ from the bulk of the
591 unretained matrix, a split peak of H₂O₂ was observed, which was closely followed by
592 unidentified negative and positive peaks, rendering the quantitative determination of
593 urinary H₂O₂ impossible, as shown in Figure 8 (b). Following this, urine samples
594 were first centrifuged at 2500 rcf for 8 min, in an attempt to remove any cellular
595 debris and heavy proteins prior to the chromatographic separation. The IC-CLD
596 chromatogram of the supernatant from the centrifuged urine samples provided a

597 smaller number of chemiluminescence peaks, as shown in Figure 8 (c), although a
598 pronounced shoulder in the H₂O₂ peak and a baseline shift were still observed (Figure
599 8 (c)). Finally, to fully precipitate all urinary proteins, 2% w/v 5-sulfosalicylic acid
600 was added to the supernatants of the centrifuged urine samples, and the solution was
601 filtered through a 0.45 μm PTFE syringe filter. IC-CLD analysis of the resultant
602 sample solutions recorded a single H₂O₂ peak and a stable baseline, as shown in
603 Figure 8 (d). Urinary H₂O₂ was then determined in three separately processed urine
604 samples (although all aliquoted from the same original sample). The urinary H₂O₂ in
605 these samples was determined to be $2.5 \pm 0.2 \mu\text{M}$, using a linear calibration plot from
606 $1.25 \mu\text{M}$ to $5 \mu\text{M}$ ($R^2 = 0.9953$). The measured urinary H₂O₂ concentration was found
607 to be in agreement with that previously reported as being typical urinary H₂O₂
608 concentrations, namely $2.7 \pm 1.2 \mu\text{M}$ ($n = 29$) in fresh urine samples, as measured by
609 a modified FOX assay [28]. As seen in the UV chromatogram in Figure 8 (d),
610 retention and co-elution of the remaining urinary components was evident, although
611 completely separated from the chemiluminescence peak of H₂O₂.

612

613 The IC-CLD setup was then applied to the determination of the H₂O₂ concentration in
614 coffee extracts. This assay did not require any prior sample preparation steps and the
615 direct IC separation of freshly brewed coffee extracts resulted in a single H₂O₂ CLD
616 peak, as shown in Figure 9. Once again the UV chromatogram shown in Figure 9
617 indicates the presence of other co-eluting coffee components. The H₂O₂ concentration
618 in three coffee extract samples was determined as being $19.6 \pm 0.3 \mu\text{M}$, using a linear
619 calibration plot from $20 \mu\text{M}$ to $80 \mu\text{M}$ ($R^2 = 0.9974$).

620



621

622 Figure 8. Effects of different sample treatment steps in the analysis of urinary H_2O_2 :

623 (a) chemiluminescence peaks obtained after direct injection of a fresh urine sample in

624 the FIA CLD system for three successive injections, (b) chemiluminescence

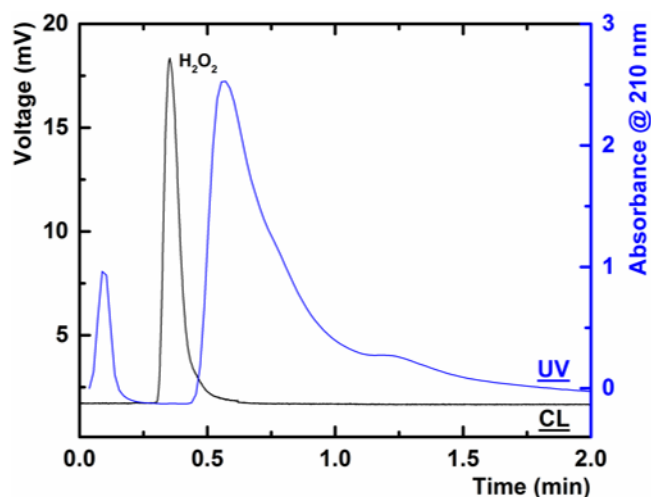
625 chromatogram obtained after direct injection of a fresh urine sample in the IC-CLD

626 system, (c) chemiluminescence chromatogram obtained after injection of the

627 supernatant from a centrifuged urine sample, and (d) chemiluminescence and UV

628 recorded chromatograms obtained after injection of a 5-sulfosalicylic acid protein

629 precipitated supernatant of a centrifuged urine sample.



630

631 Figure 9. Chemiluminescence and UV recorded chromatograms obtained after

632 injection of a fresh coffee extract sample in the IC-CLD system.

633

634 5 CONCLUSIONS

635 A new radial flow-cell design has been developed to (1) offer a less tortuous

636 alternative to the conventional chemiluminescence flow-cell designs and (2) provide a

637 higher chemiluminescence signal in terms of both the magnitude and the duration, as

638 compared to the most commonly used spiral flow-cell design. Use of the radial flow-

639 cell design enabled successful fabrication by 3D printing with closed channels for the

640 first time. Owing to the less tortuous nature of the radial flow-cell, it only required 10

641 hours of post-PolyJet print processing time as compared to ca. 360 hours required for

642 the tortuous spiral flow-cell and also facilitated a successful FDM print process. The

643 radial flow-cell design also provided higher spatial coverage near the onset of the

644 chemiluminescence reaction as compared to the spiral flow-cell design.

645 Consequentially, the radial flow-cell design resulted in ca. 60% increase in the peak

646 height and ca. 90% increase in the peak area as compared to the most commonly used

647 spiral flow-cell design and hence enabling higher sensitivity CLD. Smaller linear

648 velocities were observed in the radial flow channels as compared to the spiral flow

649 channel due to the parallel arrangement of the channels in the former. This resulted in
650 ca. 40% increase in the signal duration with the radial flow-cell design as compared to
651 the spiral flow-cell design and hence facilitating digital imaging analysis.

652

653 The 3D printed radial flow-cell was successfully applied within a novel IC-CLD
654 assay for the determination of urinary and coffee extract H₂O₂.

655

656 **6 ASSOCIATED CONTENT**

657 **6.1 Supporting Information**

658 Supplementary data associated with this article can be found, in the online version,
659 at

660

661 **7 ACKNOWLEDGMENT**

662 Funding from the Australian Research Council Centre of Excellence Scheme (Project
663 Number CE 140100012) is gratefully acknowledged. This work was also supported
664 by the Grant National Security Science and Technology Unit (NSSTU) on Counter
665 Terrorism of the Department of Prime Minister and Cabinet of Australia.

666

667

668

669

670 **8 REFERENCES**

- 671 [1] C.A. Marquette, L.J. Blum, Applications of the luminol chemiluminescent
672 reaction in analytical chemistry, *Anal. Bioanal. Chem.*, 385 (2006) 546-554.
- 673 [2] A.J. Brown, P.S. Francis, J.L. Adcock, K.F. Lim, N.W. Barnett, Manganese (III)
674 and manganese (IV) as chemiluminescence reagents: A review, *Anal. Chim. Acta*,
675 624 (2008) 175-183.
- 676 [3] J.L. Adcock, N.W. Barnett, C.J. Barrow, P.S. Francis, Advances in the use of
677 acidic potassium permanganate as a chemiluminescence reagent: a review, *Anal.*
678 *Chim. Acta*, 807 (2014) 9-28.
- 679 [4] P. Campins-Falcó, L. Tortajada-Genaro, F. Bosch-Reig, A new flow cell design
680 for chemiluminescence analysis, *Talanta*, 55 (2001) 403-413.
- 681 [5] J. Burguera, A. Townshend, S. Greenfield, Flow injection analysis for
682 monitoring chemiluminescent reactions, *Anal. Chim. Acta*, 114 (1980) 209-214.
- 683 [6] G. Rule, W.R. Seitz, Flow-injection analysis with chemiluminescence
684 detection, *Clin. Chem.*, 25 (1979) 1635-1638.
- 685 [7] H. Nakamura, Y. Murakami, K. Yokoyama, E. Tamiya, I. Karube, M. Suda, S.
686 Uchiyama, A compactly integrated flow cell with a chemiluminescent FIA system
687 for determining lactate concentration in serum, *Anal. Chem.*, 73 (2001) 373-378.
- 688 [8] É. Tyrrell, C. Gibson, B.D. MacCraith, D. Gray, P. Byrne, N. Kent, C. Burke, B.
689 Paull, Development of a micro-fluidic manifold for copper monitoring utilising
690 chemiluminescence detection, *Lab on a Chip*, 4 (2004) 384-390.
- 691 [9] Y.-X. Guan, Z.-R. Xu, J. Dai, Z.-L. Fang, The use of a micropump based on
692 capillary and evaporation effects in a microfluidic flow injection
693 chemiluminescence system, *Talanta*, 68 (2006) 1384-1389.
- 694 [10] J.M. Terry, J.L. Adcock, D.C. Olson, D.K. Wolcott, C. Schwanger, L.A. Hill, N.W.
695 Barnett, P.S. Francis, Chemiluminescence detector with a serpentine flow cell,
696 *Anal. Chem.*, 80 (2008) 9817-9821.
- 697 [11] A.M.G. Campaña, W.R. Baeyens, *Chemiluminescence in Analytical Chemistry*,
698 Marcel Dekker Incorporated 2001.
- 699 [12] S.D. Kolev, I.D. McKelvie, *Advances in flow injection analysis and related*
700 *techniques*, Elsevier 2008.
- 701 [13] N. Barnett, P. Francis, *Chemiluminescence: overview*, *Encyclopedia of*
702 *analytical science* 2005, pp. 506-511.
- 703 [14] J.L. Adcock, J.M. Terry, C.J. Barrow, N.W. Barnett, D.C. Olson, P.S. Francis,
704 *Chemiluminescence detectors for liquid chromatography*, *Drug Test Anal*, 3
705 (2011) 139-144.
- 706 [15] J.M. Terry, E.M. Zammit, T. Slezak, N.W. Barnett, D.C. Olson, D.K. Wolcott, D.L.
707 Edwards, P.S. Francis, Solution mixing and the emission of light in flow-cells for
708 chemiluminescence detection, *Analyst*, 136 (2011) 913-919.
- 709 [16] C.I. Rogers, K. Qaderi, A.T. Woolley, G.P. Nordin, 3D printed microfluidic
710 devices with integrated valves, *Biomicrofluidics*, 9 (2015) 016501.
- 711 [17] V. Gupta, M. Talebi, J. Deverell, S. Sandron, P.N. Nesterenko, B. Heery, F.
712 Thompson, S. Beirne, G.G. Wallace, B. Paull, 3D printed titanium micro-bore
713 columns containing polymer monoliths for reversed-phase liquid
714 chromatography, *Anal. Chim. Acta*, 910 (2016) 84-94.
- 715 [18] S. Sandron, B. Heery, V. Gupta, D. Collins, E. Nesterenko, P.N. Nesterenko, M.
716 Talebi, S. Beirne, F. Thompson, G.G. Wallace, 3D printed metal columns for
717 capillary liquid chromatography, *Analyst*, 139 (2014) 6343-6347.

718 [19] S. Waheed, J.M. Cabot, N.P. Macdonald, T. Lewis, R.M. Guijt, B. Paull, M.C.
719 Breadmore, 3D printed microfluidic devices: enablers and barriers, *Lab on a*
720 *Chip*, 16 (2016) 1993-2013.

721 [20] K.B. Spilstead, J.J. Learey, E.H. Doeven, G.J. Barbante, S. Mohr, N.W. Barnett,
722 J.M. Terry, R.M. Hall, P.S. Francis, 3D-printed and CNC milled flow-cells for
723 chemiluminescence detection, *Talanta*, 126 (2014) 110-115.

724 [21] K.M. Scudder, C.H. Pollema, J. Ruzicka, The fountain cell: a tool for flow-
725 based spectroscopies, *Anal. Chem.*, 64 (1992) 2657-2660.

726 [22] J.L. Perez Pavon, E. Rodriguez Gonzalo, G.D. Christian, J. Ruzicka, Universal
727 sandwich membrane cell and detector for optical flow injection analysis, *Anal.*
728 *Chem.*, 64 (1992) 923-929.

729 [23] P.K. Dasgupta, Z. Genfa, J. Li, C.B. Boring, S. Jambunathan, R. Al-Horr,
730 Luminescence detection with a liquid core waveguide, *Anal. Chem.*, 71 (1999)
731 1400-1407.

732 [24] P. Campíns-Falcó, L. Tortajada-Genaro, F. Bosch-Reig, A new flow cell design
733 for chemiluminescence analysis, *Talanta*, 55 (2001) 403-413.

734 [25] N.r. Ibáñez-García, M. Puyol, C.M. Azevedo, C.S. Martínez-Cisneros, F.
735 Villuendas, M. Gongora-Rubio, A.C. Seabra, J.n. Alonso, Vortex configuration flow
736 cell based on low-temperature cofired ceramics as a compact
737 chemiluminescence microsystem, *Anal. Chem.*, 80 (2008) 5320-5324.

738 [26] Y. Wen, H. Yuan, J. Mao, D. Xiao, M.M. Choi, Droplet detector for the
739 continuous flow luminol-hydrogen peroxide chemiluminescence system,
740 *Analyst*, 134 (2009) 354-360.

741 [27] D. Price, P.J. Worsfold, R. Fauzi, C. Mantoura, Determination of hydrogen
742 peroxide in sea water by flow-injection analysis with chemiluminescence
743 detection, *Anal. Chim. Acta*, 298 (1994) 121-128.

744 [28] J. Yuen, I. Benzie, Hydrogen peroxide in urine as a potential biomarker of
745 whole body oxidative stress, *Free Radical Res.*, 37 (2003) 1209-1213.

746 [29] S.-X. Liang, L.-X. Zhao, B.-T. Zhang, J.-M. Lin, Experimental studies on the
747 chemiluminescence reaction mechanism of carbonate/bicarbonate and
748 hydrogen peroxide in the presence of cobalt (II), *J. Phys. Chem. A*, 112 (2008)
749 618-623.

750 [30] B.C. Gross, K.B. Anderson, J.E. Meisel, M.I. McNitt, D.M. Spence, Polymer
751 coatings in 3D-printed fluidic device channels for improved cellular adherence
752 prior to electrical lysis, *Anal. Chem.*, 87 (2015) 6335-6341.

753 [31] K.B. Anderson, S.Y. Lockwood, R.S. Martin, D.M. Spence, A 3D printed fluidic
754 device that enables integrated features, *Anal. Chem.*, 85 (2013) 5622-5626.

755 [32] P. Mahbub, P. Zakaria, R. Guijt, M. Macka, G. Dicoski, M. Breadmore, P.N.
756 Nesterenko, Flow injection analysis of organic peroxide explosives using acid
757 degradation and chemiluminescent detection of released hydrogen peroxide,
758 *Talanta*, 143 (2015) 191-197.

759 [33] G.M. Greenway, T. Leelasattarakul, S. Liawruangrath, R.A. Wheatley, N.
760 Youngvises, Ultrasound-enhanced flow injection chemiluminescence for
761 determination of hydrogen peroxide, *Analyst*, 131 (2006) 501-508.

762 [34] L. Marle, G.M. Greenway, Determination of hydrogen peroxide in rainwater
763 in a miniaturised analytical system, *Anal. Chim. Acta*, 548 (2005) 20-25.

764 [35] G. De Jong, N. Lammers, F. Spruit, U.A.T. Brinkman, R. Frei, Optimization of a
765 peroxyoxalate chemiluminescence detection system for the liquid

766 chromatographic determination of fluorescent compounds, *Chromatographia*, 18
767 (1984) 129-133.

768 [36] J.M. Terry, S. Mohr, P.R. Fielden, N.J. Goddard, N.W. Barnett, D.C. Olson, D.K.
769 Wolcott, P.S. Francis, Chemiluminescence detection flow cells for flow injection
770 analysis and high-performance liquid chromatography, *Anal. Bioanal. Chem.*, 403
771 (2012) 2353-2360.

772 [37] T. Miyazawa, S. Lertsiri, K. Fujimoto, M. Oka, Luminol chemiluminescent
773 determination of hydrogen peroxide at picomole levels using high-performance
774 liquid chromatography with a cation-exchange resin gel column, *J. Chromatogr.*
775 *A*, 667 (1994) 99-104.

776 [38] S.D. Varma, P. Devamanoharan, Excretion of hydrogen peroxide in human
777 urine, *Free Radic. Res. Commun.*, 8 (1990) 73-78.

778 [39] D.-H. Wang, K. Ogino, Y. Sato, N. Sakano, M. Kubo, K. Takemoto, C. Masatomi,
779 Urinary Hydrogen Peroxide as Biomarker, *General Methods in Biomarker*
780 *Research and their Applications 2015*, pp. 313-331.

781 [40] N. Kuge, M. Kohzaki, T. Sato, Relation between natriuresis and urinary
782 excretion of hydrogen peroxide, *Free Radical Res.*, 30 (1999) 119-123.

783 [41] S. Chatterjee, A. Chen, Functionalization of carbon buckypaper for the
784 sensitive determination of hydrogen peroxide in human urine, *Biosens.*
785 *Bioelectron.*, 35 (2012) 302-307.

786 [42] L.H. Long, B. Halliwell, Coffee drinking increases levels of urinary hydrogen
787 peroxide detected in healthy human volunteers, *Free Radical Res.*, 32 (2000)
788 463-467.

789 [43] K. Hiramoto, T. Kida, K. Kikugawa, Increased urinary hydrogen peroxide
790 levels caused by coffee drinking, *Biol. Pharm. Bull.*, 25 (2002) 1467-1471.

791 [44] Y. Sato, K. Ogino, N. Sakano, D. Wang, J. Yoshida, Y. Akazawa, S. Kanbara, K.
792 Inoue, M. Kubo, H. Takahashi, Evaluation of urinary hydrogen peroxide as an
793 oxidative stress biomarker in a healthy Japanese population, *Free Radical Res.*,
794 47 (2013) 181-191.

795 [45] E. Deskur, P. Dylewicz, Ł. Szczeńniak, T. Rychlewski, M. Wilk, H. Wysocki,
796 Exercise-induced increase in hydrogen peroxide plasma levels is diminished by
797 endurance training after myocardial infarction, *Int. J. Cardiol.*, 67 (1998) 219-
798 224.

799 [46] D. Banerjee, U. Madhusoodanan, S. Nayak, J. Jacob, Urinary hydrogen
800 peroxide: a probable marker of oxidative stress in malignancy, *Clin. Chim. Acta*,
801 334 (2003) 205-209.

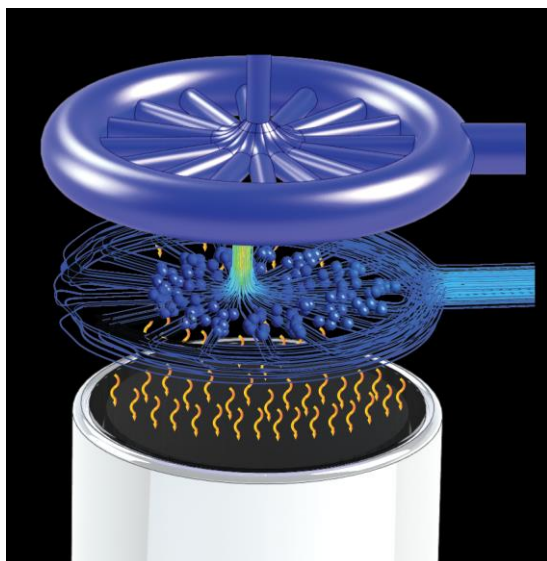
802 [47] D. Banerjee, J. Jacob, G. Kunjamma, U. Madhusoodanan, S. Ghosh,
803 Measurement of urinary hydrogen peroxide by FOX-1 method in conjunction
804 with catalase in diabetes mellitus—a sensitive and specific approach, *Clin. Chim.*
805 *Acta*, 350 (2004) 233-236.

806 [48] M. Mathru, M.W. Rooney, D.J. Dries, L.J. Hirsch, L. Barnes, M.J. Tobin, Urine
807 hydrogen peroxide during adult respiratory distress syndrome in patients with
808 and without sepsis, *Chest*, 105 (1994) 232-236.

809 [49] S. Chandramathi, K. Suresh, Z. Anita, U. Kuppusamy, Elevated levels of
810 urinary hydrogen peroxide, advanced oxidative protein product (AOPP) and
811 malondialdehyde in humans infected with intestinal parasites, *Parasitology*, 136
812 (2009) 359-363.

- 813 [50] C. Campos, R. Guzmán, E. López-Fernández, Á. Casado, Evaluation of urinary
814 biomarkers of oxidative/nitrosative stress in adolescents and adults with Down
815 syndrome, *Life Sci.*, 89 (2011) 655-661.
- 816 [51] B. Halliwell, K. Zhao, M. Whiteman, The gastrointestinal tract: a major site of
817 antioxidant action?, *Free Radical Res.*, 33 (2000) 819-830.
- 818 [52] L.H. Long, P.J. Evans, B. Halliwell, Hydrogen peroxide in human urine:
819 implications for antioxidant defense and redox regulation, *Biochem. Biophys.*
820 *Res. Commun.*, 262 (1999) 605-609.
- 821 [53] B. Halliwell, M.V. Clement, L.H. Long, Hydrogen peroxide in the human body,
822 *FEBS Lett.*, 486 (2000) 10-13.
- 823 [54] B. Halliwell, J. Gutteridge, *Oxidative stress, Free radicals in biology and*
824 *medicine*, Oxford University Press, New York, 2007, pp. 297-299.
825
826

827 **Graphical Abstract**
828



829